



Article

High-Temperature Challenges: Electrochemical Investigations into Molten Salt Corrosion Mechanisms

Fuzhen Yu, John R. Nicholls, Adrianus Indrat Aria  and Adnan U. Syed * 

Faculty of Engineering and Applied Sciences, Cranfield University, Cranfield, Bedfordshire MK43 0AL, UK

* Correspondence: adnan.syed@cranfield.ac.uk

Abstract

Thermal energy storage (TES) systems are widely employed in concentrated solar power (CSP) applications as a means of storing and dispatching energy. Typical thermal fluids used in TES systems include molten salts, such as solar salt (a $\text{KNO}_3\text{-NaNO}_3$ eutectic), as well as other inorganic salts currently under consideration. While these molten nitrate, chloride, sulfate, and carbonate salts offer favourable thermal properties, they can induce significant corrosion of metallic containment materials, leading to reduced system efficiency and component lifetime. Despite extensive post-exposure studies, in situ electrochemical understanding of corrosion mechanisms in molten solar salt remains limited, particularly for emerging alloys such as FeCrAl. In this study, the in situ corrosion behaviour of structural alloys in molten solar salt was investigated using electrochemical impedance spectroscopy (EIS). Complementary post-exposure characterization was performed using destructive techniques, including scanning electron microscopy (SEM) and energy-dispersive X-ray spectroscopy (EDX), to assess microstructural and chemical changes. The materials evaluated were stainless steel SS316 and comparatively underexplored Kanthal FeCrAl alloys, exposed to molten solar salt (40 wt% $\text{KNO}_3\text{-60 wt% NaNO}_3$) at 545 °C. The electrochemical and microstructural analyses indicate that FeCrAl exhibits superior corrosion resistance associated with the formation of a more stable and protective oxide scale, compared to SS316 under the investigated conditions. This study provides new electrochemical evidence supporting the suitability of FeCrAl alloys for TES applications, while also indicating that SS316 may develop improved corrosion resistance over extended exposure durations, highlighting the importance of long-term performance assessment.

Keywords: concentrating solar power (CSP); thermal energy storage (TES); molten salt corrosion; electrochemical characterization; solar salt



Academic Editor: Zhen Zhang

Received: 20 January 2026

Revised: 3 March 2026

Accepted: 10 March 2026

Published: 15 March 2026

Copyright: © 2026 by the authors.

Licensee MDPI, Basel, Switzerland.

This article is an open access article distributed under the terms and

conditions of the [Creative Commons Attribution \(CC BY\) license](https://creativecommons.org/licenses/by/4.0/).

1. Introduction

To address the challenges of environmental sustainability and global warming, concentrated solar power (CSP) has emerged as a promising clean energy technology. CSP installations are expected to generate a total of 2244.4 MW of electricity worldwide in 2024 [1]. A typical CSP plant consists of solar concentrators, receivers, heat transfer and storage media, and power conversion systems [2]. Among these components, thermal energy storage (TES) has become a critical element of CSP plants and the broader renewable energy infrastructure [3]. TES enables CSP facilities to generate electricity during periods of high solar irradiance and to continue power production after sunset by maintaining elevated operating temperatures. This capability mitigates intermittency associated with solar resources and allows CSP plants, when integrated with TES, to function as near-continuous

power generation systems. Furthermore, CSP systems equipped with TES offer greater operational flexibility compared to other renewable technologies, such as solar photovoltaics, by compensating for short-term fluctuations in energy availability [4].

Molten salts play a central role in TES applications due to their favourable thermal properties and suitability for high-temperature operation. In active TES systems, molten salts are commonly used as heat transfer fluids (HTFs), circulating through the system to enable charging and discharging of stored thermal energy, while in passive storage systems, the HTF transfers heat to a dedicated storage medium [2]. Active TES systems can be further classified into direct and indirect configurations. In direct systems, the HTF also serves as the storage medium and is heated directly within the solar field. In contrast, indirect systems utilize the HTF solely for heat transport, with thermal energy transferred to the storage medium via a heat exchanger. In both configurations, cold and hot storage media are typically separated into two dedicated tanks or into two distinct regions within a single tank [5]. Among these designs, two-tank molten salt systems have demonstrated greater thermal stability and have been successfully implemented in several commercial CSP plants, particularly in parabolic trough configurations. However, the operating temperatures of these systems are generally limited to below 600 °C, primarily due to materials and corrosion constraints [5].

Molten salts are used as the sensible or latent heat media for the TES applications. Nitrate salts have been commonly applied as an efficient working fluid for CSP systems, which can increase electrical efficiency and reduce the levelized cost of electricity (LCOE) [6]. The binary mixture of 60% NaNO₃ + 40% KNO₃ can store solar energy for up to 15 h for commercial CSP plants [7–10].

The melting point of traditional solar salt is around 240 °C and the thermal stability limit is approx. 565 °C; the protective gas that reduces the decomposition loss can increase the operation temperature limit to 600 °C [11–14]. Research has been set out to find the decomposition of sodium and potassium nitrates [15]. Yang et al. [16] studied NO_x emissions of the ternary molten nitrate salts (HITEC) used in TES. Moreover, Cristina et al. [17] studied the influence of the decomposition of the solar salt from the impurity magnesium. These studies aimed at the effect of solar salt in contact with the container material.

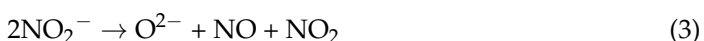
Corrosion in molten nitrates usually stems from the corrosive ions in the molten salt, such as oxides and nitrites, which separate from the nitrate anions [18]. Molten nitrate salts, particularly eutectic mixtures such as NaNO₃–KNO₃ (solar salt), are widely used as heat transfer and thermal energy storage media in concentrated solar power (CSP) systems due to their favourable thermophysical properties. However, at elevated operating temperatures (typically above 500–550 °C), these salts undergo partial thermal decomposition, leading to the formation of chemically reactive species that significantly influence corrosion behaviour of structural alloys. The primary decomposition pathway of nitrate ions involves their reduction to nitrite ions with the release of oxygen gas [14,19–21].



As temperature increases further, nitrite ions themselves become thermodynamically unstable and decompose according to



In addition to gaseous nitrogen oxides, nitrite decomposition contributes to the formation of oxide ions within the molten salt



The generation of oxide ions (O^{2-}) is particularly important from a corrosion perspective, as it increases the basicity of the molten salt. Elevated oxide activity alters the oxygen chemical potential of the melt and promotes destabilization of protective oxide scales formed on metallic components. Despite the extensive literature on molten nitrate corrosion, most studies rely on ex situ techniques such as mass change measurements and post-exposure characterization. While informative, these approaches do not capture the dynamic electrochemical and oxide scale evolution occurring during high-temperature exposure. Consequently, in situ electrochemical insight into corrosion mechanisms under CSP-relevant molten salt conditions remains limited. Structural alloys exposed to molten nitrate salts typically rely on the formation of protective oxide layers, such as Cr_2O_3 on stainless steels or Al_2O_3 on FeCrAl alloys. However, oxide ions present in the molten salt can chemically interact with these protective layers through basic fluxing mechanisms, leading to scale thinning or dissolution. Representative reactions may be expressed as:



Such reactions result in the dissolution of the oxide scale into the molten salt, thereby reducing its protective effectiveness and exposing the underlying metal to continued oxidation and corrosion. The presence of nitrogen oxides (NO and NO_2) further contributes to fluctuations in local oxygen partial pressure, which can disrupt scale adherence and promote non-protective oxide growth.

The corrosion rate of structural alloys in molten nitrate salts is primarily governed by the nitrate–nitrite equilibrium and the stability of the protective oxide scale formed on the alloy surface [22]. In nitrate melts, oxide scales can dissolve via fluxing mechanisms, resulting in the progressive depletion of thermodynamically stable oxide-forming elements such as chromium and aluminum [23]. Numerous studies have reported significantly higher corrosion rates for low-chromium steels exposed to molten solar salt when compared with austenitic stainless steels [23–26]. Low-carbon chromium steels, in particular, exhibit distinctive corrosion behaviour characterized by the rapid onset of breakaway corrosion, leading to the formation of thick, multi-layered, and non-protective oxide scales. These corrosion products predominantly consist of sodium ferrite ($NaFeO_2$) and hematite (Fe_2O_3), which provide limited protection against further degradation [20].

Overall, high-temperature corrosion processes in molten salt environments are complex and strongly influenced by dynamic chemical equilibria within the melt. Conventional corrosion rate measurement techniques typically rely on ex situ mass change analysis following predetermined exposure periods [23–27]. While informative, such approaches are time-consuming and do not capture the evolving chemistry and kinetics occurring during active corrosion. Consequently, increasing attention has been directed toward electrochemical techniques to establish correlations between in situ electrochemical signals and corrosion state. Most recent studies have focused on the relationship between polarization behaviour and corrosion rate in molten salt systems [28,29].

In particular, FeCrAl alloys remain comparatively underexplored in molten nitrate-based TES systems when compared with conventional austenitic stainless steels such as SS316. The Al_2O_3 -based protection mechanism in FeCrAl differs fundamentally from the Cr_2O_3 -dominated behaviour of stainless steels, yet their relative electrochemical performance in molten solar salt has not been systematically evaluated. This study addresses this gap through in situ electrochemical impedance spectroscopy (EIS) supported by post-exposure microstructural analysis.

2. Materials and Methods

2.1. Salt Preparation

The solar salt mixture was prepared by blending potassium nitrate (KNO_3) and sodium nitrate (NaNO_3). KNO_3 ($\geq 99.0\%$ purity) was procured from Sigma-Aldrich (Burlington, MA, USA), and NaNO_3 ($\geq 99.0\%$ purity) was supplied by Thermo Scientific (Waltham, MA, USA). To simulate a typical thermal energy storage (TES) molten salt used in concentrated solar power (CSP) applications, the salt composition was fixed at 40 wt% KNO_3 and 60 wt% NaNO_3 .

According to the literature [14], solar salt with this composition exhibits a melting point of approximately 240°C and a thermal stability limit in the range of $530\text{--}565^\circ\text{C}$, with a specific heat capacity of approximately $1.5\text{ kJ kg}^{-1}\text{ K}^{-1}$.

Prior to testing, the salts were thoroughly mixed and dried in air at 120°C for 12 h to remove moisture and water of crystallization. Approximately 8 g of the dried salt mixture was then transferred into an alumina crucible. The crucible containing the salt was kept in the drying oven at 120°C until the start of the corrosion experiments to minimize moisture uptake.

2.2. Alloy Preparation

In this study, stainless steel 316 (SS316) and FeCrAl alloys, supplied by Goodfellow Advanced Materials, (Huntingdon, UK) were evaluated for 80 h exposure in molten solar salt. The chemical compositions and dimensions of the alloys are summarized in Tables 1 and 2 respectively. Figure 1 shows the molten salt corrosion rig after machining, which was used for in situ corrosion testing.

Table 1. Composition of SS316 and FeCrAl alloy.

Alloy	Composition [wt%]						
	Fe	Ni	Cr	Mn	Mo	Si	Al
SS316	67.71	9.55	18.87	1.14	1.53	1.20	
FeCrAl	67.55	-	21.44	-	-	-	11.01

Table 2. Size and surface area of the tested sample.

Alloy	Size Parameter [mm]			Surface Area [cm^2]
	Length	Width	Thickness (Average)	
SS316	11.66	12.60	3.03	4.41
FeCrAl	12.37	11.16	2.03	3.72

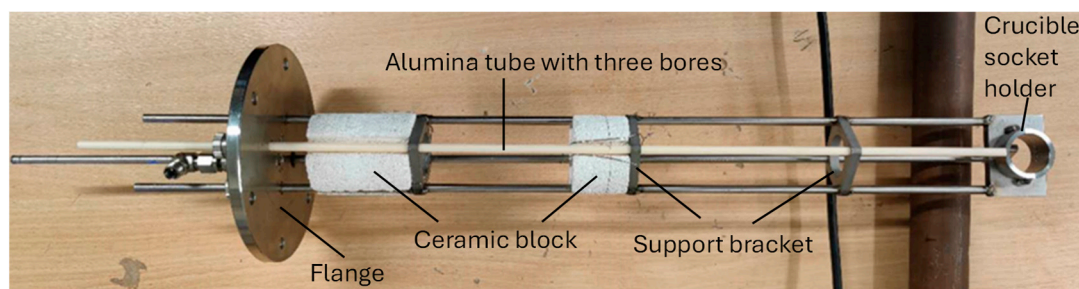


Figure 1. Molten salt corrosion rig for in situ electrochemical tests.

Each sample was mounted as the working electrode (WE) in a three-electrode electrochemical setup. Electrical connection was established using a $0.5\text{ mm Ni}_{80}/\text{Cr}_{20}$ wire

(Goodfellow Advanced Materials), which was insulated with application of silicon dioxide cement CEMEX, (Rugby, UK) shown in Figure 2 to define the exposed surface area and eliminate the influence of the connecting wire.



Figure 2. Applying cement coating to the sample to cover the wire connection.

Prior to testing, the sample surfaces and wires were polished using silicon carbide (SiC) sandpaper to achieve a smooth, uniform finish. The working electrode, along with the counter (CE) and reference electrodes (RE), was assembled in a custom-designed rig. Electrochemical measurements were performed using a three-electrode configuration. The alloy sample served as the working electrode. A platinum wire mounted at the tip of a Ni-80Cr-20 (Nichrome) lead was used as a quasi-reference electrode, while a separate platinum wire of larger surface area, similarly mounted on a Ni-80Cr-20 lead, was employed as the counter electrode.

2.3. Electrochemical Test

Figure 3 provides an overview of the corrosion rig: panel (a) shows the complete three-electrode setup with supporting rig components, while panel (b) presents a close-up of the counter, reference, and working electrodes fully immersed in the prepared molten salt contained within an alumina crucible prior to the start of the experiment.

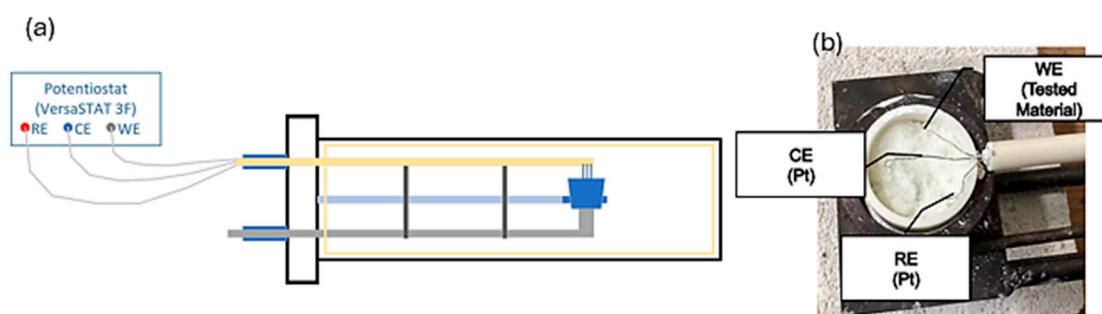


Figure 3. (a) Schematic of the three-electrode electrochemical setup with potentiostat, showing the RE (reference electrode), CE (counter electrode), and WE (working electrode) (b) Photograph of the assembled molten salt sample prior to exposure, showing electrodes and wires inserted into the salt within the crucible, housed in an alumina three-bore tube.

Electrochemical measurements were performed using a VersaSTAT 3F potentiostat system (TN, US), including open-circuit potential (OCP) monitoring and electrochemical

impedance spectroscopy (EIS). The samples were exposed to molten solar salt at 545 °C, representing the typical operating temperature of molten solar salt in CSP thermal energy storage systems under an argon atmosphere for 80 h, with EIS data collected every 20 h throughout the exposure period. The measurements correspond to a single continuous exposure experiment for each alloy, and the results presented in this work are representative time-resolved data acquired at 20, 40, 60, and 80 h. EIS measurements were carried out at OCP at exposure times using a frequency range from 100 kHz to 100 mHz with an AC perturbation amplitude of 10 mV. One data point per decade was recorded across the investigated frequency range.

Ni₈₀/Cr₂₀ wires served as long conducting leads drawn into alumina tube bores, with platinum used at the tips as the counter (CE) and reference (RE) electrodes. Stainless steel 316 (SS316) and FeCrAl alloys were used as the working electrodes (WE). At each electrode junction—including Pt and Ni₈₀/Cr₂₀ for the CE and RE, and Ni₈₀/Cr₂₀ connected to the target working electrode (SS316 or FeCrAl)—cement was applied to prevent cross-contamination between different metal chemistries.

The test conditions, including temperature, furnace environment, and intervals of electrochemical data acquisition via EIS, are summarized in Table 3: Molten salt corrosion test matrix.

Table 3. Molten salt corrosion test matrix.

Parameter	Setting/Period
Testing Temperature	545 °C
Testing Environment	Argon
1st EIS Measurement	20 h (total time 20 h)
2nd EIS Measurement	20 h (total time 40 h)
3rd EIS Measurement	20 h (total time 60 h)
4th EIS Measurement	20 h (total time 80 h)

Electrochemical techniques commonly employed in molten salt corrosion studies include potentiodynamic polarization (PDP), open-circuit potential (OCP) monitoring, and electrochemical impedance spectroscopy (EIS). These methods have been widely reported for in situ corrosion assessment and online degradation monitoring, notably in studies by Vidal et al. at NREL (USA) [3] and Bonk et al. at DLR (Germany) [10]. Among these techniques, EIS is particularly valuable for probing corrosion mechanisms through impedance responses associated with charge-transfer processes and the integrity of protective surface layers.

In the present work, the focus is placed exclusively on EIS measurements as an initial investigation following the development of a custom-designed molten salt corrosion rig at Cranfield University (UK). The primary objective is to analyze Nyquist impedance responses and their evolution as a function of alloy composition and exposure duration in molten salt environments. Changes in impedance characteristics are interpreted in terms of corrosion degradation behaviour, including charge-transfer resistance and the possible breakdown of passive or semi-protective surface layers.

The relationship between EIS-derived parameters and corrosion rate is a key aspect of in situ molten salt corrosion monitoring, providing insight into time-dependent degradation processes under high-temperature conditions. Accordingly, this study reports EIS results as an indicator of relative corrosion resistance for different alloys over extended exposure periods.

Further work will expand this electrochemical framework by incorporating potentiodynamic polarization testing to generate Tafel plots and extract quantitative corrosion parameters, enabling a more comprehensive evaluation of corrosion kinetics and mechanisms in molten salt environments.

2.4. Microscopy Analysis

Following electrochemical testing, polished cross-sectional sample mounts were prepared for destructive post-exposure analysis. Sample preparation involved mounting, sectioning, grinding, and polishing using standard metallographic procedures.

The polished cross sections were first examined at the macroscopic scale to evaluate corrosion morphology using a digital microscope Keyence VHX-7000 (Milton Keynes, UK). High-resolution microstructural characterization of the cross sections was subsequently performed using scanning electron microscopy (SEM). SEM analyses were conducted using a TESCAN VEGA3 microscope (Kohoutovice, Czech Republic) equipped with a backscattered electron (BSE) detector and energy-dispersive X-ray spectroscopy (EDX), operating at an accelerating voltage of 20 kV.

3. Result and Discussion

3.1. Electrochemistry Analysis

Open-circuit potential (OCP) represents the mixed potential spontaneously established at the metal–electrolyte interface and reflects the dynamic balance between anodic oxidation and cathodic reduction reactions occurring on the metal surface. As such, OCP measurements are widely used to assess corrosion tendency and interfacial stability. A shift of the OCP towards more negative values generally indicates surface activation, often associated with the destabilization or rupture of passive films, leading to enhanced anodic dissolution and increased corrosion susceptibility. In contrast, a shift towards more positive potentials is typically linked to the formation or stabilization of protective surface layers and/or enhanced cathodic reactions, resulting in improved corrosion resistance. When the OCP attains a stable value, it suggests that the interfacial electrochemical processes have approached a quasi-steady-state condition.

As shown in the OCP evolution in Figure 4, both SS316 and the FeCrAl alloy exhibit a rapid initial shift towards more negative potentials upon exposure to the molten salt, indicating pronounced surface activation and the onset of corrosion reactions. This initial transient behaviour is followed by potential fluctuations, reflecting a dynamic interplay between oxide layer breakdown and reformation as the metal–salt interface evolves. After approximately 50 h of exposure, the OCP values of both materials (measured versus the Pt reference electrode) stabilize, signifying the establishment of steady interfacial conditions. Notably, FeCrAl reaches this stable potential more rapidly and maintains comparatively less negative OCP values than SS316, consistent with the formation of a more stable and protective Al- and Cr-rich surface layer. In contrast, the delayed stabilization observed for SS316 suggests prolonged surface activation and reduced corrosion resistance under the tested molten salt conditions.

Figure 5 shows the EIS plots of the SS316 and FeCrAl. The two materials exhibit similar frequency response trends in their signal behaviour. The Nyquist plots can be equivalent to the internal resistance of molten salt and two interfaces representing the oxide–electrolyte interface and metal–electrolyte interface. In the EIS plots, the size of the semicircle for both materials decreases as the testing time increases, which is reflected in the equivalent circuit in which the equivalent resistance of the oxide–electrolyte interface and metal–electrolyte interface shows a resistance decrease as time goes by. By comparing the variation trends of

the semicircle sizes in the EIS plots of the two materials, it can be roughly estimated that the semicircle size in the EIS plot of FeCrAl decreases at a faster rate.

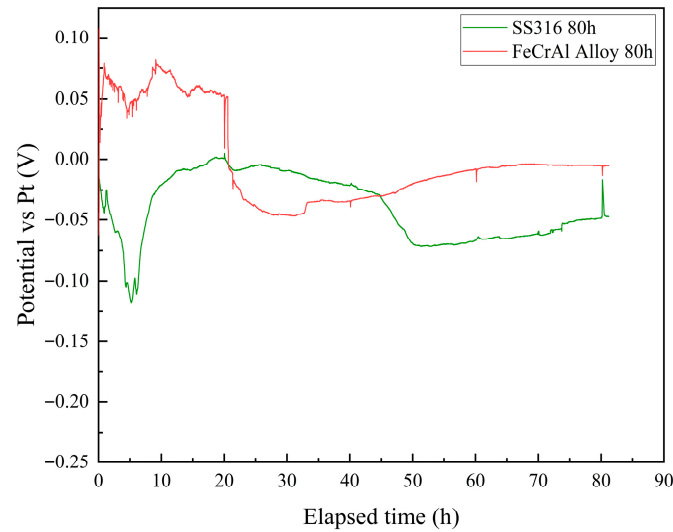


Figure 4. Open-circuit potential (OCP) evolution of SS316 and FeCrAl alloys measured versus a Pt quasi-reference electrode during 80 h exposure in molten solar salt at 545 °C under argon atmosphere.

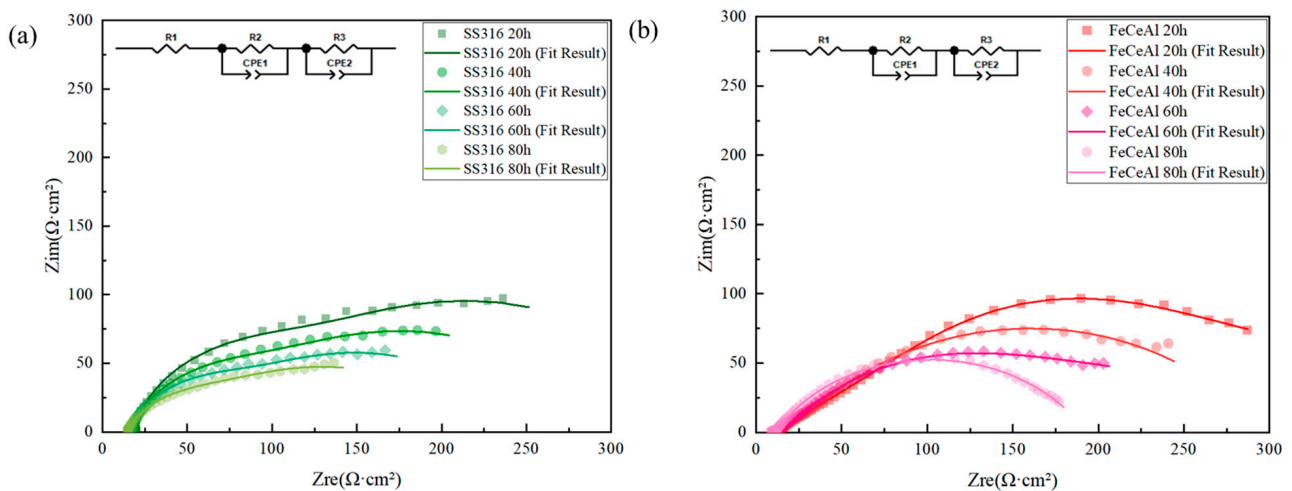


Figure 5. Nyquist plots obtained from electrochemical impedance spectroscopy (EIS) measurements of (a) SS316 and (b) FeCrAl alloys after 20, 40, 60, and 80 h exposure in molten solar salt at 545 °C. Symbols represent experimental data and solid lines indicate fitted results using the equivalent electrical circuit shown.

Table 4 shows the data of the components in an equivalent circuit diagram. R_1 represents the internal resistance of molten salt, R_2 represents the resistance of the oxide–electrolyte interface, and R_3 represents the resistance of the metal–electrolyte interface. It can be found that during the 80 h test, the resistance of the metal–electrolyte interface of the FeCrAl alloy is greater than SS316, which means in this period FeCrAl alloy has a better corrosion resistance than SS316. However, by analyzing the tendency of the Nyquist plots, it can be discovered that the resistance change in the metal–electrolyte interface of the FeCrAl alloy ($86 \Omega \cdot \text{cm}^2$) is greater than SS316 ($70.9 \Omega \cdot \text{cm}^2$). Hence, a longer period experiment, for example, more than 800 h exposure experiment, should be set up to verify if the FeCrAl alloy has a better corrosion resistance than SS316.

Table 4. The Component Data of the Equivalent Circuit in 80 h Exposure Test.

	ET/h	$R_1/\Omega \cdot \text{cm}^2$	$R_2/\Omega \cdot \text{cm}^2$	$R_3/\Omega \cdot \text{cm}^2$	$\text{CPE1}/\text{F} \cdot \text{cm}^2 \cdot \text{s}^{(a1-1)}$	a1	$\text{CPE2}/\text{F} \cdot \text{cm}^2 \cdot \text{s}^{(a2-1)}$	a2
FeCrAl Alloy	20	11.28	69.47	267.7	2.730×10^{-3}	0.43	3.416×10^{-3}	1
	40	10.90	20.36	264.3	2.934×10^{-3}	0.45	1.664×10^{-3}	0.65
	60	8.99	21.43	239.1	5.363×10^{-3}	0.40	2.112×10^{-3}	0.74
	80	8.35	2.778	181.7	1.726×10^{-2}	0.25	2.189×10^{-3}	0.56
SS316	20	18.78	98.71	228.4	5.042×10^{-3}	0.82	1.126×10^{-3}	0.90
	40	17.31	75.33	194.4	1.151×10^{-3}	0.86	4.903×10^{-3}	0.76
	60	15.82	64.10	161.5	1.401×10^{-3}	0.85	6.805×10^{-3}	0.73
	80	14.2	45.95	157.5	2.236×10^{-3}	0.78	7.884×10^{-3}	0.65

3.2. Microscopy and Damage Measurement

The microstructural and compositional evolution of SS316 and FeCrAl alloys after exposure to molten solar salt at 545 °C was evaluated using SEM coupled with EDS. Figure 6 shows the cross-sectional SEM images and corresponding EDS elemental maps, while Tables 5 and 6 present the quantitative atomic percentages of selected regions (spectra) for each alloy.

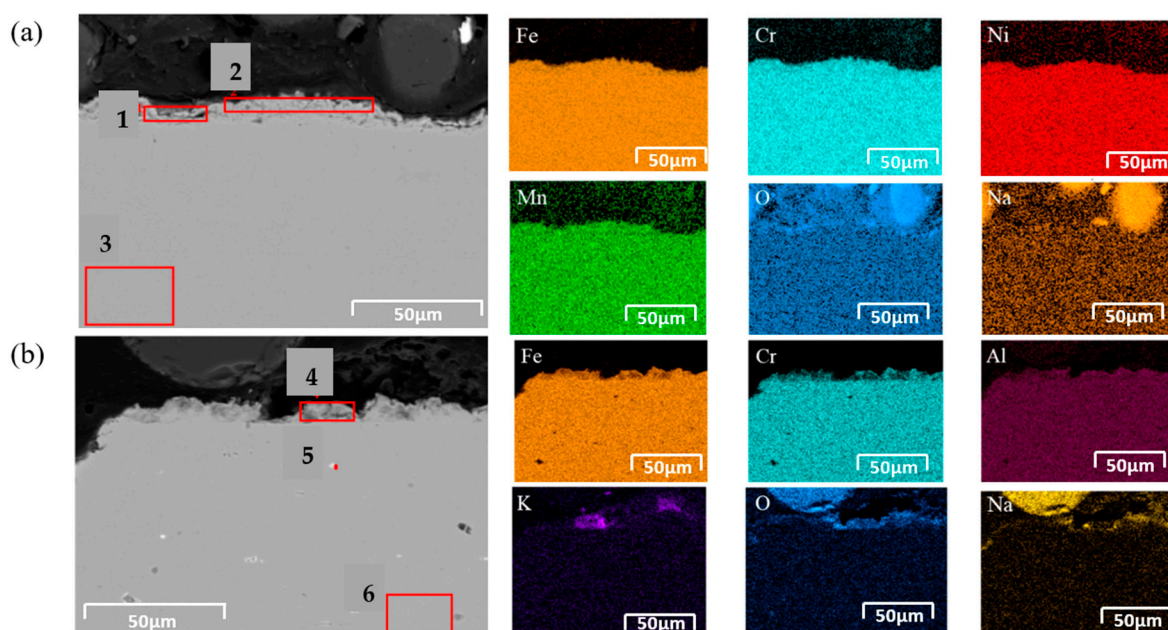


Figure 6. SEM cross-sectional images and corresponding EDS elemental maps of (a) SS316 and (b) FeCrAl alloys after 80 h exposure to molten solar salt at 545 °C. The highlighted regions indicate areas selected for EDS analysis provided in Figures 6a and 6b in Tables 5 and 6 respectively.

Table 5. EDX elemental composition (at.%) of SS316 measured for selected regions after 80 h exposure to molten solar salt at 545 °C.

Spectra Label	O	Na	Si	K	Cr	Mn	Fe	Ni	Mo	Total
1	53.23	0.55	1.48	0.08	8.05	0.48	31.16	4.35	0.63	100.00
2	53.88	0.55	5.45	0.09	6.55	0.43	28.96	4.02	0.63	100.00
3	1.11	0.05	1.51	-	18.18	1.10	68.13	8.72	1.20	100.00

Table 6. EDX elemental composition (at.%) of FeCrAl measured for selected regions after 80 h exposure to molten solar salt at 545 °C.

Spectra Label	N	O	Na	Al	Si	K	Cr	Fe	Total
4	21.83	62.53	11.53	-	0.01	3.91	0.05	0.15	100.00
5	1.90	50.67	0.77	0.16	0.08	11.12	8.53	26.76	100.00
6	0.05	3.74	0.03	9.25	0.28	0.07	20.22	66.36	100.00

3.2.1. SS316 Alloy

The SEM image of SS316 (Figure 6a) reveals the presence of surface pits, as highlighted by arrows, which are indicative of localized corrosion. The EDS maps show significant oxygen enrichment near the surface, accompanied by Fe, Cr, and Ni, suggesting the formation of a mixed oxide layer. Sodium and minor silicon are detected along the surface edges, consistent with residual molten salt deposits.

Quantitative EDX analysis (Table 5) confirms these observations. Spectra 1 and 2, corresponding to the surface oxide, contain high oxygen content (53.23–53.88 at.%) and notable Fe (\approx 29–31 at.%), Cr (\approx 6–8 at.%), and Ni (\approx 4 at.%). In contrast, spectrum 3, representing the bulk substrate, shows minimal oxygen (1.11 at.%) and a composition dominated by Fe (68.13 at.%), Cr (18.18 at.%), and Ni (8.72 at.%). The presence of Na (\approx 0.55 at.%) and Si (up to 5.45 at.%) in the surface oxide indicates partial salt penetration, which can destabilize the oxide and contribute to pitting. These results suggest that the surface oxidation of SS316 is relatively heterogeneous and provides limited protection against continued corrosion. Similar behaviour has been reported in previous studies on austenitic stainless steels in molten salt environments [3,6].

3.2.2. FeCrAl Alloy

In contrast, the FeCrAl alloy exhibits a more uniform and adherent surface oxide (Figure 6b). The EDS maps indicate aluminum enrichment within the oxide layer, along with oxygen, confirming the formation of a protective alumina-rich scale. Residual Na and K are present only at trace levels on the extreme surface.

Table 6 shows that spectrum 4, corresponding to the outermost layer, contains high oxygen (62.53 at.%) and nitrogen (21.83 at.%), exhibits to the surface region containing residual molten salt deposits, which contributes to the elevated nitrogen signal. Spectrum 5, representing the intermediate oxide, has substantial oxygen (50.67 at.%) and contributions from Fe (26.76 at.%), Cr (8.53 at.%), and minor Al (0.16 at.%), indicating the formation of a stable Fe–Cr–Al mixed oxide. The substrate (spectrum 6) remains largely unoxidized, with low oxygen (3.74 at.%) and high Fe (66.36 at.%), Cr (20.22 at.%), and Al (9.25 at.%).

This composition confirms that aluminum plays a critical role in stabilizing the oxide layer, resulting in effective passivation and suppression of further corrosion, consistent with electrochemical measurements showing a more positive corrosion potential than SS316. Similar protective behaviour of FeCrAl alloys in high-temperature molten salts has been documented in the literature [30,31].

4. Comparative Discussion

The combined SEM and EDX results demonstrate a clear difference in corrosion behaviour between the two alloys. While both alloys form surface oxides, the SS316 oxide is heterogeneous, partially contaminated with residual salts, and prone to pitting. In contrast, the FeCrAl alloy develops a dense, aluminum-assisted oxide layer that limits oxygen ingress and improves overall corrosion resistance. These microstructural observations are consistent with electrochemical measurements; open-circuit potential (OCP) shows that

FeCrAl exhibits a more positive corrosion potential and lower corrosion current densities than SS316.

Furthermore, EIS results provide additional insight into the protective nature of the oxide layers. The FeCrAl alloy exhibits higher charge-transfer resistance (R_{ct}) and larger impedance modulus at low frequencies compared with SS316, indicating a more compact and adherent passive layer that effectively impedes ion transport. In contrast, the lower impedance and less capacitive response of SS316 reflect its heterogeneous, porous oxide, which is less effective at preventing electrolyte penetration and localized corrosion. The EIS analysis therefore quantitatively supports the SEM/EDS observations, confirming that aluminum enrichment and the formation of a stable Fe–Cr–Al oxide layer are critical for enhanced corrosion resistance in molten solar salt environments.

5. Conclusions

According to the electrochemistry and SEM results after an 80 h solar salt corrosion test can draw out these conclusions as follows.

- After 50 h of exposure to molten solar salt at 545 °C, FeCrAl stabilized at ~+22 mV, whereas SS316 reached −39 mV, indicating a more noble and corrosion-resistant surface for FeCrAl.
- FeCrAl exhibits higher charge-transfer resistance throughout the 80 h test compared with SS316, reflecting superior passivation. The observed decrease in resistance over time suggests that neither alloy reached a fully stable oxide layer, highlighting the need for longer-term studies.
- SEM/EDS observations show both alloys form thin surface oxide layers during exposure. SS316 shows heterogeneous oxides and pronounced pitting, whereas FeCrAl develops a dense, aluminum-assisted oxide that effectively limits oxygen ingress and substrate degradation.
- Aluminum plays a critical role in forming a protective Fe–Cr–Al oxide layer, which accounts for the superior corrosion resistance of FeCrAl under high-temperature molten salt conditions.
- These results indicate that FeCrAl and other aluminum-containing alloys are promising candidates for structural materials in high-temperature concentrated solar power (CSP) and thermal energy storage applications.

Further work should include longer exposure durations to assess long-term passivation stability, incorporation of additional Tafel plots and EIS studies over time, evaluation of other candidate alloys, and testing across broader salt compositions and temperature ranges to simulate more realistic operational conditions.

Author Contributions: F.Y.: Methodology, Investigation, Visualization, Writing—original draft, Data curation, Formal analysis. J.R.N.: Supervision, Writing—review and editing. A.I.A.: Conceptualization, Supervision, Writing—review and editing. A.U.S.: Methodology, Conceptualization, Validation, Visualization, Supervision, Formal analysis, Writing—review and editing. All authors have read and agreed to the published version of the manuscript.

Funding: This research received no external funding.

Data Availability Statement: Data will be made available on request.

Acknowledgments: The authors would like to thank Alejandro Pacheco Nunez and Cameron Davis for their assistance with laboratory experiments and testing. Their support in conducting the experimental work is gratefully acknowledged.

Conflicts of Interest: The authors declare no conflict of interest.

References

1. IRENA. *Innovation Outlook: Thermal Energy Storage*; International Renewable Energy Agency: Abu Dhabi, United Arab Emirates, 2020.
2. Gil, A.; Medrano, M.; Martorell, I.; Lázaro, A.; Dolado, P.; Zalba, B.; Cabeza, L.F. State of the art on high temperature thermal energy storage for power generation. Part 1—Concepts, Concepts, materials and modellization. *Renew. Sustain. Energy Rev.* **2010**, *14*, 31–55. [[CrossRef](#)]
3. Gomez-Vidal, J.; Tirawat, R. Corrosion of alloys in a chloride molten salt (NaCl-LiCl) for solar thermal technologies. *Sol. Energy Mater. Sol. Cells* **2016**, *157*, 234–244. [[CrossRef](#)]
4. Denholm, P.; Mehos, M. Enabling Greater Penetration of Solar Power via the Use of CSP with Thermal Energy Storage. In *Concentrating Solar Power: Data and Directions for an Emerging Solar Technology*; National Renewable Energy Laboratory: Golden, CO, USA, 2011. [[CrossRef](#)]
5. Kuravi, S.; Trahan, J.; Goswami, D.Y.; Rahman, M.M.; Stefanakos, E.K. Thermal energy storage technologies and systems for concentrating solar power plants. *Prog. Energy Combust. Sci.* **2013**, *39*, 285–319. [[CrossRef](#)]
6. Fernández, A.G.; Muñoz-Sánchez, B.; Nieto-Maestre, J.; García-Romero, A. High temperature corrosion behavior on molten nitrate salt-based nanofluids for CSP plants. *Renew. Energy* **2019**, *130*, 902–909. [[CrossRef](#)]
7. Fernández, A.; Ushak, S.; Galleguillos, H.; Pérez, F. Development of new molten salts with LiNO₃ and Ca(NO₃)₂ for energy storage in CSP plants. *Appl. Energy* **2014**, *119*, 131–140. [[CrossRef](#)]
8. Yasir, S.; Endrino, J.L.; Guillén, E.; Aria, A.I. Suppression of molten salt corrosion by plasma sprayed Ni₃Al coatings. *Emergent Mater.* **2021**, *4*, 1583–1593. [[CrossRef](#)]
9. Lai, G.Y. Molten Salt Corrosion. In *High-Temperature Corrosion and Materials Applications*; ASM International: Materials Park, OH, USA, 2007; Chapter 15; pp. 409–421.
10. Porcayo-Calderon, J.; Sotelo-Mazon, O.; Salinas-Bravo, V.M.; Arrieta-Gon-Gonzalez, C.D.; Ramos-Hernandez, J.J.; Cuevas-Arteaga, C. Electrochemical performance of Ni20Cr coatings applied by combustion powder spray in ZnCl₂-KCl molten salts. *Int. J. Electrochem. Sci.* **2012**, *7*, 1134–1148. [[CrossRef](#)]
11. Porcayo-Calderón, J.; Sotelo-Mazón, O.; Casales-Díaz, M.; Ascencio-Gutiérrez, J.A.; Salinas-Bravo, V.M.; Martínez-Gómez, L. Electrochemical Study of Ni20Cr Coatings Applied by HVOF Process in ZnCl₂-KCl at High Temperatures. *J. Anal. Methods Chem.* **2014**, *2014*, 1–10. [[CrossRef](#)]
12. Barraza-Fierro, J.I.; Espinosa-Medina, M.A.; Hernandez-Hernandez, M.; Liu, H.B.; Sosa-Hernandez, E. Effect of Li and Cu addition on corrosion of Fe–40 at.% Al intermetallics in molten LiCl–KCl eutectic salt. *Corros. Sci.* **2012**, *59*, 119–126. [[CrossRef](#)]
13. Cuevas-Arteaga, C.; Uruchurtu-Chavarín, J.; Porcayo-Calderon, J.; Izquierdo-Montalvo, G.; Gonzalez, J. Study of molten salt corrosion of HK-40m alloy applying linear polarization resistance and conventional weight loss techniques. *Corros. Sci.* **2004**, *46*, 2663–2679. [[CrossRef](#)]
14. Bonk, A.; Braun, M.; Sötz, V.A.; Bauer, T. Solar Salt—Pushing an old material for energy storage to a new limit. *Appl. Energy* **2020**, *262*, 114535. [[CrossRef](#)]
15. Wei, X.; Wang, Y.; Peng, Q.; Yang, J.; Ding, J. NO_x emissions and NO₂- formation in thermal energy storage process of binary molten nitrate salts. *Energy* **2014**, *74*, 215–221. [[CrossRef](#)]
16. Yang, C.; Wei, X.; Wang, W.; Lin, Z.; Ding, J.; Wang, Y.; Peng, Q.; Yang, J. NO_x emissions and the component changes of ternary molten nitrate salts in thermal energy storage process. *Appl. Energy* **2016**, *184*, 346–352. [[CrossRef](#)]
17. Prieto, C.; Ruiz-Cabaas, F.J.; Rodríguez-Sánchez, A.; Abujás, C.R.; Cabeza, L.F. Effect of the impurity magnesium nitrate in the thermal decomposition of the solar salt. *Sol. Energy* **2018**, *192*, 186–192. [[CrossRef](#)]
18. Klotz, U.E.; Solenthaler, C.; Uggowitzer, P.J. Martensitic–austenitic 9–12% Cr steels—Alloy design, microstructural stability and mechanical properties. *Mater. Sci. Eng. A* **2008**, *476*, 186–194. [[CrossRef](#)]
19. Nissen, D.A. *The Chemistry of the Binary NaNO₃-KNO₃ System*; No. SAND 81-8007; Sandia National Laboratories Albuquerque: Albuquerque, NM, USA, 1981.
20. Audigié, P.; Bizien, N.; Baráibar, I.; Rodríguez, S.; Pastor, A.; Hernández, M.; Agüero, A. Aluminide slurry coatings for protection of ferritic steel in molten nitrate corrosion for concentrated solar power technology. *AIP Conf. Proc.* **2017**, *1850*, 1.
21. Giuliano, S.; Puppe, M.; Frantz, C.; Uhlig, R.; Flesch, R.; Baumann, T.; Schmalz, S.; Ibraheem, W.; Engelhard, M.; Guder, C.; et al. *HPMS-High Performance Molten Salt Tower Receiver System*; Deutsches Zentrum für Luft: Stuttgart, Germany, 2017.
22. Slusser, J.W.; Titcomb, J.B.; Heffelfinger, M.T.; Dunbobbin, B.R. Corrosion in molten nitrate-nitrite salts. *J. Miner. Met. Mater. Soc.* **1985**, *37*, 24–27. [[CrossRef](#)]
23. Audigié, P.; Encinas-Sánchez, V.; Juez-Lorenzo, M.; Rodríguez, S.; Gutiérrez, M.; Pérez, F.J.; Agüero, A. High temperature molten salt corrosion behavior of aluminide and nickel-aluminide coatings for heat storage in concentrated solar power plants. *Surf. Coat. Technol.* **2018**, *349*, 1148–1157. [[CrossRef](#)]
24. Fernández, A.G.; Lasanta, M.I.; Pérez, F.J. Molten salt corrosion of stainless steels and low-cr steel in csp plants. *Oxid. Met.* **2012**, *78*, 329–348. [[CrossRef](#)]

25. Spiegel, M.; Mentz, J. High temperature corrosion beneath nitrate melts. *Mater. Corros.* **2014**, *65*, 276–281. [[CrossRef](#)]
26. Summers, K.L.; Chidambaram, D. Corrosion behavior of structural materials for potential use in nitrate salts based solar thermal power plants. *J. Electrochem. Soc.* **2017**, *164*, H5357–H5363. [[CrossRef](#)]
27. Espinosa-Medina, M.A.; Carbajal-De la Torre, G.; Liu, H.B.; Martínez-Villafañe, A.; González-Rodríguez, J.G. Hot corrosion behaviour of Fe–Al based intermetallic in molten NaVO₃ salt. *Corros. Sci.* **2009**, *51*, 1420–1427. [[CrossRef](#)]
28. Trevani, I.N.; Calvo, E.; Corti, H.R. Diffusion coefficients of iodide in high temperature aqueous solutions. *Electrochem. Commun.* **2000**, *2*, 312–316. [[CrossRef](#)]
29. Trevani, L.N.; Calvo, E.; Corti, H.R. High-temperature wall-tube cell Design, characterization and results of mass transport phenomena. *J. Chem. Soc. Faraday Trans.* **1997**, *93*, 4319–4326. [[CrossRef](#)]
30. Marcus, P.; Oudar, J. (Eds.) *Corrosion Mechanisms in Theory and Practice*; Marcel Dekker: New York, NY, USA, 2002.
31. Zhang, S.; Hayashi, S.; Ukai, S. High-temperature oxidation of oxide-dispersion-strengthened FeCrAl alloys: Influences of Al, Co and Y concentration on the mechanism of oxide scale growth. *J. Mater. Res. Technol.* **2024**, *30*, 9196–9204. [[CrossRef](#)]

Disclaimer/Publisher’s Note: The statements, opinions and data contained in all publications are solely those of the individual author(s) and contributor(s) and not of MDPI and/or the editor(s). MDPI and/or the editor(s) disclaim responsibility for any injury to people or property resulting from any ideas, methods, instructions or products referred to in the content.

High-temperature challenges: electrochemical investigations into molten salt corrosion mechanisms

Yu, Fuzhen

2026-03

Attribution 4.0 International

Yu F, Nicholls JR, Aria AI, Syed AU. (2026) High-temperature challenges: electrochemical investigations into molten salt corrosion mechanisms. *Crystals*, Volume 16, Issue 3, March 2026, Article number 200

<https://doi.org/10.3390/cryst16030200>

Downloaded from CERES Research Repository, Cranfield University